Engineering Analysis with Boundary Elements 60 (2015) 123–136

Contents lists available at ScienceDirect

Engineering Analysis with Boundary Elements

journal homepage: www.elsevier.com/locate/enganabound

Method of fundamental solutions for 3D elasticity with body forces by coupling compactly supported radial basis functions

Cheuk-Yu Lee [a], Hui Wang [a,b], Qing-Hua Qin [a,*]

[a] Research School of Engineering, Australian National University, Acton, ACT 2601, Australia
[b] Department of Engineering Mechanics, Henan University of Technology, Zhengzhou 450001, China

ARTICLE INFO

Article history:
Received 3 November 2014
Received in revised form
15 December 2014
Accepted 19 December 2014
Available online 21 January 2015

Keywords:
Three-dimensional linear elasticity
Method of fundamental solutions
Particular solutions
Compactly supported radial basis functions

ABSTRACT

In this paper, a meshless computational model by integrating the method of fundamental solutions (MFS) and the method of particular solutions fulfilled with compactly supported radial basis functions (CSRBF) is developed for three-dimensional (3D) linear elasticity with the presence of body forces. The corresponding displacement and stress particular solution kernels across the support radius are firstly derived using Galerkin vectors and then are used to modify the boundary conditions. Subsequently, the classical meshless MFS, in which the homogeneous part of the full solutions are approximated using the linear combination of displacement and stress fundamental solutions in 3D linear elasticity, is formulated for solving the homogeneous 3D linear elastic system. Finally, several examples are presented to demonstrate the accuracy and efficiency of the present meshless method and also the effect of sparseness of interpolation matrix in CSRBF interpolation is discussed.

1. Introduction

Due to the presence of inhomogeneous body force terms, which may be caused by the gravitational forces and inertial forces, the particular solutions for 3D isotropic linear elasticity problems are of great importance when more precise stress analysis is required in 3D bodies where two-dimensional (2D) or axisymmetric or plane stress analyses are not feasible. Apart from analytical solutions which are available only for a few problems with simple geometries and boundary conditions [1–6], numerical methods such as the finite element method (FEM), the finite difference method (FDM) and the boundary element/integral method (BEM/BIM) provide alternative approaches to approximate the 3D elasticity solutions in the past decades [7–10]. Among them, the FEM and the FDM require domain discretisation while the BEM/BIM requires only boundary discretisation for the homogeneous partial differential equations (PDE) and domain discretisation for the inhomogeneous PDE respectively. In order to simplify the domain discretisation in BEM for inhomogeneous cases, the dual reciprocity method (DRM) [11] has been commonly employed to avoid the domain integration by applying collocation discretisation in the domain. This is done by approximating the inhomogeneous terms by a series of linearly independent basis functions and then analytically determines the respected particular solution kernels. The choice of the basis functions is critical to provide accurate numerical solutions [12]. In most of the literatures, the usual choices are the radial basis function (RBF). Successful RBF applications to 3D linear elasticity problems include the globally supported Gaussian [13], power splines and thin plate splines [14].

The severe drawback of using the above globally supported RBFs is their dense interpolation matrices, which often become highly ill-conditioned as the number of interpolation points or the order of basis functions increases. Conversely, RBFs with local support such as the Wendland's CSRBF are capable of producing sparse interpolation matrices and improving matrix conditioning while maintaining competitive accuracy [15–17]. As the result, CSRBF has become a natural choice for solving higher dimensional problems [18–20]. To our best knowledge, the application of the CSRBF has only been applied to 2D elasticity problems by Rashed [21,22].

In this paper, a mixed meshless collocation method by integrating the homogeneous and particular solutions is developed for 3D linear elasticity with the presence of body forces. Similar approach had also been made in Galerkin meshless method for solving isotropic elasticity and anisotropic plate problems [23,24]. In our approach, we consider using MFS for the approximation of homogeneous terms and the method of particular solutions fulfilled with CSRBF instead of the conventional globally supported basis functions for the approximation of inhomogeneous terms. During the computation, we can freely control the sparseness of the interpolation matrix by varying the support radius without trading off too much of the accuracy. Using Galerkin vectors in the linear elastic theory, the particular solution

* Corresponding author.
E-mail address: qinghua.qin@anu.edu.au (Q.-H. Qin).

http://dx.doi.org/10.1016/j.enganabound.2014.12.009
0955-7997/

kernels with respect to the CSRBF approximation are firstly derived and then the displacement and stress particular solutions are obtained to modify the boundary conditions. Subsequently, the homogeneous solutions are evaluated by the MFS using the modified boundary conditions. Finally, several examples are presented to demonstrate the accuracy and efficiency of the present method.

The remainder of this paper is organised as follows. Section 2 describes the basics of three-dimensional elasticity. Section 3 presents the derivation of the particular solution kernels associated with the Wendland's CSRBF, and in Section 4, the method of fundamental solutions is presented for the homogeneous terms. Several examples are considered in Section 5 and a further discussion on the sparseness of the CSRBF is given in Section 6. Finally, some concluding remarks on the present method are presented in Section 7.

2. Problem description

Consider a 3D isotropic linear elastic body with inhomogeneous terms in the domain Ω. The governing equations are

$$\sigma_{ij,j}(X)+b_i(X)=0, \quad X\in\Omega \tag{1}$$

$$\sigma_{ij}(X)=\lambda\varepsilon_{kk}(X)\delta_{ij}+2G\varepsilon_{ij}(X), \quad X\in\Omega \tag{2}$$

$$\varepsilon_{ij}(X)=\tfrac{1}{2}\left(u_{i,j}(X)+u_{j,i}(X)\right), \quad X\in\Omega \tag{3}$$

where σ_{ij} is the stress tensor, ε_{ij} the strain tensor, u_i the displacement vector, b_i the known body force vector, λ and G the Lame constants and δ the Kronecker delta.

Combining the above equations yields the following Navier's equations in terms of displacement components

$$Gu_{i,jj}(X)+\frac{G}{1-2\nu}u_{j,ij}(X)+b_i(X)=0, \quad X\in\Omega \tag{4}$$

where ν is Poisson's ratio which can be expressed as $\nu=\lambda/(2(\lambda+G))$. Later in the numerical examples, Young modulus E and ν will be employed, in which G can be computed using the conversion formula $G=E/(2(1+\nu))$.

The corresponding boundary conditions are

- Dirichlet/necessary condition

$$u_i(X)=\bar{u}_i(X), \quad X\in\Gamma_u \tag{5a}$$

- Neumann boundary condition

$$t_i(X)=\sigma_{ij}(X)n_j(X)=\bar{t}_i(X), \quad X\in\Gamma_t \tag{5b}$$

where t_i is the traction field, $\bar{u}_i$ and $\bar{t}_i$ the prescribed displacement and traction, n_i the unit vector outward normal to $\Gamma=\Gamma_u\cup\Gamma_t$.

3. Method of particular solutions

Using the method of particular solutions, the full solution variables u_i can be expressed as the sum of particular solutions u_i^p and homogeneous solutions u_i^h [23,24], that is

$$u_i(X)=u_i^p(X)+u_i^h(X), \quad X\in\Omega \tag{6}$$

where u_i^p should satisfy the inhomogeneous equation (4) and u_i^h satisfies the homogeneous equations with modified boundary conditions:

$$Gu_{i,jj}^h(X)+\frac{G}{1-2\nu}u_{j,ij}^h(X)=0, \quad X\in\Omega \tag{7}$$

$$u_i^h(X)=\bar{u}_i(X)-u_i^p(X), \quad X\in\Gamma_u \tag{8a}$$

$$t_i^h(X)=\bar{t}_i(X)-t_i^p(X), \quad X\in\Gamma_t \tag{8b}$$

In order to determine the particular solution, it is convenient to express the particular solutions of displacement u_i^p in terms of Galerkin vector g_i as [25]

$$u_i^p(X)=g_{i,kk}(X)-\frac{1}{2(1-\nu)}g_{k,ik}(X), \quad X\in\Omega \tag{9}$$

Upon substituting Eq. (9) into Eq. (4) yields the following biharmonic equation

$$g_{i,jjkk}(X)=-\frac{b_i(X)}{G}, \quad X\in\Omega \tag{10}$$

By means of derivation of displacement variables, the corresponding stress particular solutions in terms of Galerkin vector is

$$\sigma_{ij}(X)=\frac{G}{1-\nu}\left[\nu g_{k,mmk}(X)\delta_{ij}-g_{k,ijk}(X)+(1-\nu)\left(g_{i,jkk}(X)+g_{j,ikk}(X)\right)\right], \quad X\in\Omega \tag{11}$$

3.1. Dual reciprocity method

Sometimes, inhomogeneous terms of Eq. (10) could be a well described function such as gravitational load, for which special particular solution can be found analytically [26]. In many other cases, finding such analytical solution is not a trivial task. The dual reciprocity method aims to efficiently approximate the particular solution by finding its solution kernels while prescribing the inhomogeneous terms such as body forces with a series of linearly independent basis functions so that any known or unknown body force terms can be reconstructed using finite set of discrete data

$$b_i(X)\approx\sum_{n=1}^{N}\alpha_l^n\delta_{li}\varphi_n(X), \quad X\in\Omega \tag{12a}$$

where φ_n is the chosen series of functions to approximate body forces from the inhomogeneity terms of Eq. (10), N the number of interpolation points in the domain, α_l^n the interpolation coefficients to be determined. The use of the Kronecker delta δ is to separate the basis functions for approximating the body forces in each direction independently, i.e.

$$\begin{bmatrix} \varphi_1(X) & 0 & 0 & \varphi_2(X) & 0 & 0 & \cdots & \varphi_N(X) & 0 & 0 \\ 0 & \varphi_1(X) & 0 & 0 & \varphi_2(X) & 0 & \cdots & 0 & \varphi_N(X) & 0 \\ 0 & 0 & \varphi_1(X) & 0 & 0 & \varphi_2(X) & \cdots & 0 & 0 & \varphi_N(X) \end{bmatrix} \begin{Bmatrix} \alpha_1^1 \\ \alpha_2^1 \\ \alpha_3^1 \\ \alpha_1^2 \\ \alpha_2^2 \\ \alpha_3^2 \\ \vdots \\ \alpha_1^N \\ \alpha_2^N \\ \alpha_3^N \end{Bmatrix} = \begin{Bmatrix} b_1(X) \\ b_2(X) \\ b_3(X) \end{Bmatrix} \tag{12b}$$

Similarly, the Galerkin vector g_i and the particular solution u_i^p and σ_{ij}^p can be expressed as

$$g_i(X) = \sum_{n=1}^{N} \alpha_l^n \delta_{li} \phi_n(X), \quad X \in \Omega \tag{13a}$$

$$u_i^p(X) = \sum_{n=1}^{N} \alpha_l^n \psi_{li}^n(X), \quad X \in \Omega \tag{13b}$$

$$\sigma_{ij}^p(X) = \sum_{n=1}^{N} \alpha_l^n S_{lij}^n(X), \quad X \in \Omega \tag{13c}$$

where ϕ_n is the respected Galerkin vector solution kernels, ψ_{li}^n the displacement particular solution kernels, S_{lij}^n the stress particular solution kernels.

By linearity, it suffices to analytically determine ϕ_n by substituting Eqs. (12) and (13a) into Eq. (10)

$$\phi_{n,jjkk}(X) = -\frac{\varphi_n(X)}{G}, \quad X \in \Omega \tag{14}$$

It is clear that by enforcing Eq. (10) to satisfy the known inhomogeneity terms in Ω, we can obtain N linear equations to uniquely solve for the interpolation coefficients α_l^n.

3.2. Particular solution kernels with CSRBF

Generally, the function φ in Eq. (14) can be chosen as radial basis function such that

$$\varphi_j(X_i) = \varphi(||X_i - X_j||) = \varphi(r_{ij}) \tag{15}$$

where X_i represents the collocation points and X_j represents the reference points.

Herein, RBF is employed to approximate the inhomogeneous terms of Eq. (10), as done in some literatures [19,22,27,28]. Since RBF is expressed in terms of Euclidian distance, it usually works well in arbitrary dimensional space and does not increase computational cost. Furthermore, many attractive properties of RBF such as good convergence power, positive definiteness and ease of smoothness control are widely reported [29,30].

Then, from Eqs. (9), (13a), (13b) the displacement particular solution kernels can be expressed as

$$\psi_{li}(r) = \delta_{li}\phi_1 - \frac{1}{2(1-\nu)}(\delta_{li}\phi_2 + r_{,i}r_{,l}\phi_3) \tag{16}$$

Similarly, the stress particular solution kernels can be expressed as

$$S_{lij}(r) = \frac{G}{1-\nu}\left(\left[\delta_{ij}r_{,l}\nu + (1-\nu)(\delta_{li}r_{,j} + \delta_{lj}r_{,i})\right]\phi_4 - (\delta_{lj}r_{,i} + \delta_{li}r_{,j} + \delta_{ij}r_{,l})\phi_5 - r_{,i}r_{,j}r_{,l}\phi_6\right) \tag{17}$$

where

$$\phi_1 = \phi_{,rr} + \frac{2}{r}\phi_{,r} \tag{18a}$$

$$\phi_2 = \frac{1}{r}\phi_{,r} \tag{18b}$$

$$\phi_3 = \phi_{,rr} - \frac{1}{r}\phi_{,r} \tag{18c}$$

$$\phi_4 = \phi_{,rrr} + \frac{2}{r}\phi_{,rr} - \frac{2}{r^2}\phi_{,r} \tag{18d}$$

$$\phi_5 = \frac{1}{r}\phi_{,rr} + \frac{1}{r^2}\phi_{,r} \tag{18e}$$

$$\phi_6 = \phi_{,rrr} - \frac{3}{r}\phi_{,rr} + \frac{3}{r^2}\phi_{,r} \tag{18f}$$

To analytically determine ϕ, ψ_{li} and S_{lij}, an explicit function needs to be chosen first for φ. For Wendland's CSRBF in 3D [16,17], φ is defined as

For C^0 smoothness

$$\varphi(r) = \left(1 - \frac{r}{\alpha}\right)_+^2 = \begin{cases} \left(1 - \frac{r}{\alpha}\right)^2, & 0 \le r \le \alpha, \\ 0, & r > \alpha, \end{cases} \tag{19a}$$

For C^2 smoothness

$$\varphi(r) = \left(1 - \frac{r}{\alpha}\right)_+^4 \left(4\frac{r}{\alpha} + 1\right) \tag{19b}$$

For C^4 smoothness

$$\varphi(r) = \left(1 - \frac{r}{\alpha}\right)_+^6 \left(35\left(\frac{r}{\alpha}\right)^2 + 18\frac{r}{\alpha} + 3\right) \tag{19c}$$

For C^6 smoothness

$$\varphi(r) = \left(1 - \frac{r}{\alpha}\right)_+^8 \left(35\left(\frac{r}{\alpha}\right)^3 + 25\left(\frac{r}{\alpha}\right)^2 + 8\frac{r}{\alpha} + 1\right) \tag{19d}$$

where the subscript $+$ denotes that the bracket function will be forced to be zero when the bracketed value is less than zero. α is a cut off parameter for varying the support radius of interpolation matrix $\varphi(r)$ as illustrated in Fig. 1.

The sparseness of the CSRBF interpolation matrix can be interpreted as the cumulative frequency of r, which is defined as

$$sparseness = \sum_{i}^{N}\sum_{j}^{N} f(r_{ij})\,[r_{ij} \le \alpha] \tag{20a}$$

with

$$f(r) = \sum_{i}^{N}\sum_{j}^{N} \frac{[r = r_{ij}]}{N^2} \tag{20b}$$

where f is the frequency function of r_{ij} and $[\cdot]$ denotes the use of Iverson Bracket. For case $\alpha = \max(r)$, sparseness of the interpolation matrix is equal to 100%. For case $\alpha = 0$, the sparseness is equal to 0%. In practice α can be chosen according to the sparseness requirement.

Since the radial part of the bi-harmonic operator in Eq. (14) can be written as

$$\nabla^4 = \frac{\partial^4}{\partial r^4} + \frac{4}{r}\frac{\partial^3}{\partial r^3} \tag{21}$$

the Galerkin vector solution kernels ϕ can be analytically determined for points located within the compact support radius by solving the ordinary differential equation

$$\frac{\partial^4\phi(r)}{\partial r^4} + \frac{4}{r}\frac{\partial^3\phi(r)}{\partial r^3} = -\frac{\varphi(r)}{G} \quad \text{for } 0 \le r \le \alpha \tag{22}$$

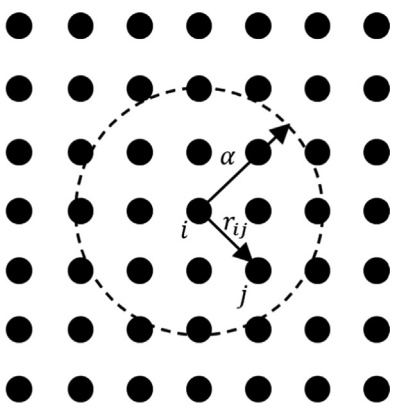

Fig. 1. Cut off parameter α for various support radii.

For points located outside the compact support radius, ϕ satisfies the homogeneous equation (24)

$$\frac{\partial^4\phi(r)}{\partial r^4}+\frac{4}{r}\frac{\partial^3\phi(r)}{\partial r^3}=0 \quad \text{for } r>\alpha \tag{23}$$

with solution

$$\phi_{r>\alpha}(r)=C_1r^2+C_2r+C_3+\frac{C_4}{r} \tag{24}$$

The four constants C_1, C_2, C_3, C_4 are to be chosen so that ϕ satisfies the continuity conditions at the compact support radius, that is

$$\phi_{r>\alpha}(\alpha)=\phi_{0\le r\le\alpha}(\alpha) \tag{25a}$$

$$\phi'_{r>\alpha}(\alpha)=\phi'_{0\le r\le\alpha}(\alpha) \tag{25b}$$

$$\phi''_{r>\alpha}(\alpha)=\phi''_{0\le r\le\alpha}(\alpha) \tag{25c}$$

$$\phi'''_{r>\alpha}(\alpha)=\phi'''_{0\le r\le\alpha}(\alpha) \tag{25d}$$

Particularly, the corresponding ϕ for the first three Wendland's CSRBF defined in Eqs. (19a–19c) are expressed in Eqs. (26a), (27a), (28a) for points located within the compact support radius and in Eqs. (26b), (27b), (28b) for points located outside the compact support radius.

- For C^0 smoothness

$$\phi_{0\le r\le\alpha}=-\frac{r^4}{120G}+\frac{r^5}{180G\alpha}-\frac{r^6}{840G\alpha^2} \tag{26a}$$

$$\phi_{r>\alpha}=\frac{\alpha^5}{630Gr}-\frac{\alpha^4}{120G}+\frac{\alpha^3r}{60G}-\frac{\alpha^2r^2}{72G} \tag{26b}$$

- For C^2 smoothness

$$\phi_{0\le r\le\alpha}=-\frac{r^4}{120G}+\frac{r^6}{84G\alpha^2}-\frac{r^7}{84G\alpha^3}+\frac{5r^8}{1008G\alpha^4}-\frac{r^9}{1260G\alpha^5} \tag{27a}$$

$$\phi_{r>\alpha}=\frac{\alpha^5}{1260Gr}-\frac{5\alpha^4}{1008G}+\frac{\alpha^3r}{84G}-\frac{\alpha^2r^2}{84G} \tag{27b}$$

- For C^4 smoothness

$$\phi_{0\le r\le\alpha}=-\frac{r^4}{40G}+\frac{r^6}{30G\alpha^2}-\frac{5r^8}{72G\alpha^4}+\frac{4r^9}{45G\alpha^5}-\frac{7r^{10}}{132G\alpha^6}+\frac{8r^{11}}{495G\alpha^7}-\frac{7r^{12}}{3432G\alpha^8} \tag{28a}$$

$$\phi_{r>\alpha}=\frac{8\alpha^5}{6435Gr}-\frac{7\alpha^4}{792G}+\frac{4\alpha^3r}{165G}-\frac{\alpha^2r^2}{36G} \tag{28b}$$

It should be noted that the ϕ across the support radius are at least thrice differentiable for the minimal smoothness of the CSRBF as evidenced by Eqs. (24) and (26a). By substituting Eqs. (26)–(28) into Eqs. (16)–(18), the displacement and stress particular solution kernels can be found:

- For C^0 smoothness

$$\psi_{li,0\le r\le\alpha}(r)=-\frac{r^2(84r_{,i}r_{,l}-378\delta_{li}+420\delta_{li}\nu)}{2520G(\nu-1)}-\frac{r^2(126\delta_{li}r^2\nu-117\delta_{li}r^2+36r_{,i}r_{,l}r^2)}{2520G\alpha^2(\nu-1)}+\frac{\alpha r^2(105r_{,i}r_{,l}r-385\delta_{li}r+420\delta_{li}r\nu)}{2520G\alpha^2(\nu-1)} \tag{29a}$$

$$\psi_{li,r>\alpha}(r)=\frac{\alpha^2(175\delta_{li}-210\delta_{li}\nu)}{2520G(\nu-1)}-\frac{\alpha^2(2\alpha^3\delta_{li}-6\alpha^3r_{,i}r_{,l})}{2520Gr^3(\nu-1)}-\frac{\alpha^2r^2(63\alpha\delta_{li}+21\alpha r_{,i}r_{,l}-84\alpha\delta_{li}\nu)}{2520Gr^3(\nu-1)} \tag{29b}$$

$$S_{lij,0\le r\le\alpha}(r)=-\frac{r(\delta_{li}r_{,j}-\delta_{ij}r_{,l}+\delta_{lj}r_{,i})(10\alpha^2-15\alpha r+6r^2)}{30\alpha^2}-\frac{r(28\alpha^2\delta_{li}r_{,j}-112\alpha^2\delta_{ij}r_{,l}+28\alpha^2\delta_{lj}r_{,i}-72\delta_{ij}r_{,l}r^2+12\delta_{li}r_{,j}r^2+12\delta_{lj}r_{,i}r^2)}{420\alpha^2(\nu-1)}-\frac{r(24r_{,i}r_{,j}r_{,l}r^2+175\alpha\delta_{ij}r_{,l}r-35\alpha\delta_{li}r_{,j}r-35\alpha\delta_{lj}r_{,i}r-35\alpha r_{,i}r_{,j}r_{,l}r)}{420\alpha^2(\nu-1)} \tag{29c}$$

$$S_{lij,r>\alpha}(r)=\frac{\alpha^3(\delta_{li}r_{,j}-\delta_{ij}r_{,l}+\delta_{lj}r_{,i}+3r_{,i}r_{,j}r_{,l}+2\delta_{ij}r_{,l}\nu-2\delta_{li}r_{,j}\nu-2\delta_{lj}r_{,i}\nu)}{60r^2(\nu-1)}+\frac{\alpha^5(\delta_{ij}r_{,l}+\delta_{li}r_{,j}+\delta_{lj}r_{,i}-5r_{,i}r_{,j}r_{,l})}{210r^4(\nu-1)} \tag{29d}$$

- For C^2 smoothness

$$\psi_{li,0\le r\le\alpha}(r)=-\frac{r^2(84r_{,i}r_{,l}-378\delta_{li}+420\delta_{li}\nu)}{2520G(\nu-1)}-\frac{r^2(180\delta_{li}r^5\nu-171\delta_{li}r^5+63r_{,i}r_{,l}r^5)}{2520G\alpha^5(\nu-1)}+\frac{\alpha r^2(900\delta_{li}r^4\nu-850\delta_{li}r^4+300r_{,i}r_{,l}r^4)}{2520G\alpha^5(\nu-1)}+\frac{\alpha^3r^2(1260\delta_{li}r^2\nu-1170\delta_{li}r^2+360r_{,i}r_{,l}r^2)}{2520G\alpha^5(\nu-1)}-\frac{\alpha^2r^2(1680\delta_{li}r^3\nu-1575\delta_{li}r^3+525r_{,i}r_{,l}r^3)}{2520G\alpha^5(\nu-1)} \tag{30a}$$

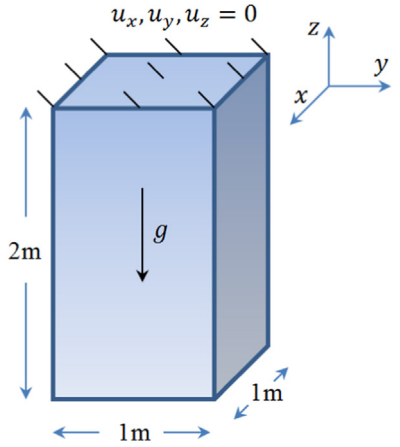

Fig. 2. Prismatic bar under gravitational load.

$$\psi_{li,r>\alpha}(r)=\frac{\alpha^2(150\delta_{li}-180\delta_{li}\nu)}{2520G(\nu-1)}-\frac{\alpha^2(\alpha^3\delta_{li}-3\alpha^3 r_{,i}r_{,l})}{2520Gr^3(\nu-1)}-\frac{\alpha^2 r^2(45\alpha\delta_{li}+15\alpha r_{,i}r_{,l}-60\alpha\delta_{li}\nu)}{2520Gr^3(\nu-1)} \tag{30b}$$

$$\psi_{li,r>\alpha}(r)=\frac{\alpha^2(3575\delta_{li}-4290\delta_{li}\nu)}{25740G(\nu-1)}-\frac{\alpha^2(16\alpha^3\delta_{li}-48\alpha^3 r_{,i}r_{,l})}{25740Gr^3(\nu-1)}-\frac{\alpha^2 r^2(936\alpha\delta_{li}+312\alpha r_{,i}r_{,l}-1248\alpha\delta_{li}\nu)}{25740Gr^3(\nu-1)} \tag{31b}$$

$$\begin{aligned}S_{lij,0\le r\le\alpha}(r)=&-\frac{r(\delta_{li}r_{,j}-\delta_{ij}r_{,l}+\delta_{lj}r_{,i})(14\alpha^5-84\alpha^3r^2+140\alpha^2r^3-90\alpha r^4+21r^5)}{42\alpha^5}\\&-\frac{r\left(28\alpha^5\delta_{li}r_{,j}-112\alpha^5\delta_{ij}r_{,l}+28\alpha^5\delta_{lj}r_{,i}-189\delta_{ij}r_{,l}r^5+21\delta_{li}r_{,j}r^5+21\delta_{lj}r_{,i}r^5+800\alpha\delta_{ij}r_{,l}r^4\right)}{420\alpha^5(\nu-1)}\\&-\frac{r\left(-100\alpha\delta_{li}r_{,j}r^4-100\alpha\delta_{lj}r_{,i}r^4+105r_{,i}r_{,j}r_{,l}r^5-1225\alpha^2\delta_{ij}r_{,l}r^3+175\alpha^2\delta_{li}r_{,j}r^3+175\alpha^2\delta_{lj}r_{,i}r^3\right)}{420\alpha^5(\nu-1)}\\&-\frac{r\left(720\alpha^3\delta_{ij}r_{,l}r^2-120\alpha^3\delta_{li}r_{,j}r^2-120\alpha^3\delta_{lj}r_{,i}r^2+525\alpha^2r_{,i}r_{,j}r_{,l}r^3-240\alpha^3r_{,i}r_{,j}r_{,l}r^2-400\alpha r_{,i}r_{,j}r_{,l}r^4\right)}{420\alpha^5(\nu-1)}\end{aligned} \tag{30c}$$

$$\begin{aligned}S_{lij,0\le r\le\alpha}(r)=&\frac{4r^3(\delta_{ij}r_{,l}-6\delta_{li}r_{,j}-6\delta_{lj}r_{,i}+2r_{,i}r_{,j}r_{,l}-7\delta_{ij}r_{,l}\nu+7\delta_{li}r_{,j}\nu+7\delta_{lj}r_{,i}\nu)}{5\alpha^2(\nu-1)}\\&-\frac{r(\delta_{ij}r_{,l}-4\delta_{li}r_{,j}-4\delta_{lj}r_{,i}-5\delta_{ij}r_{,l}\nu+5\delta_{li}r_{,j}\nu+5\delta_{lj}r_{,i}\nu)}{5(\nu-1)}\\&-\frac{10r^5(\delta_{ij}r_{,l}-8\delta_{li}r_{,j}-8\delta_{lj}r_{,i}+4r_{,i}r_{,j}r_{,l}-9\delta_{ij}r_{,l}\nu+9\delta_{li}r_{,j}\nu+9\delta_{lj}r_{,i}\nu)}{3\alpha^4(\nu-1)}\\&+\frac{28r^6(\delta_{ij}r_{,l}-9\delta_{li}r_{,j}-9\delta_{lj}r_{,i}+5r_{,i}r_{,j}r_{,l}-10\delta_{ij}r_{,l}\nu+10\delta_{li}r_{,j}\nu+10\delta_{lj}r_{,i}\nu)}{5\alpha^5(\nu-1)}\\&-\frac{140r^7(\delta_{ij}r_{,l}-10\delta_{li}r_{,j}-10\delta_{lj}r_{,i}+6r_{,i}r_{,j}r_{,l}-11\delta_{ij}r_{,l}\nu+11\delta_{li}r_{,j}\nu+11\delta_{lj}r_{,i}\nu)}{33\alpha^6(\nu-1)}\\&+\frac{8r^8(\delta_{ij}r_{,l}-11\delta_{li}r_{,j}-11\delta_{lj}r_{,i}+7r_{,i}r_{,j}r_{,l}-12\delta_{ij}r_{,l}\nu+12\delta_{li}r_{,j}\nu+12\delta_{lj}r_{,i}\nu)}{5\alpha^7(\nu-1)}\\&-\frac{35r^9(\delta_{ij}r_{,l}-12\delta_{li}r_{,j}-12\delta_{lj}r_{,i}+8r_{,i}r_{,j}r_{,l}-13\delta_{ij}r_{,l}\nu+13\delta_{li}r_{,j}\nu+13\delta_{lj}r_{,i}\nu)}{143\alpha^8(\nu-1)}\end{aligned} \tag{31c}$$

$$S_{lij,r>\alpha}(r)=\frac{\alpha^3(\delta_{li}r_{,j}-\delta_{ij}r_{,l}+\delta_{lj}r_{,i}+3r_{,i}r_{,j}r_{,l}+2\delta_{ij}r_{,l}\nu-2\delta_{li}r_{,j}\nu-2\delta_{lj}r_{,i}\nu)}{84r^2(\nu-1)}+\frac{\alpha^5(\delta_{ij}r_{,l}+\delta_{li}r_{,j}+\delta_{lj}r_{,i}-5r_{,i}r_{,j}r_{,l})}{420r^4(\nu-1)} \tag{30d}$$

$$S_{lij,r>\alpha}(r)=\frac{4\alpha^3(\delta_{li}r_{,j}-\delta_{ij}r_{,l}+\delta_{lj}r_{,i}+3r_{,i}r_{,j}r_{,l}+2\delta_{ij}r_{,l}\nu-2\delta_{li}r_{,j}\nu-2\delta_{lj}r_{,i}\nu)}{165r^2(\nu-1)}+\frac{8\alpha^5(\delta_{ij}r_{,l}+\delta_{li}r_{,j}+\delta_{lj}r_{,i}-5r_{,i}r_{,j}r_{,l})}{2145r^4(\nu-1)} \tag{31d}$$

- For C^4 smoothness

$$\begin{aligned}\psi_{li,0\le r\le\alpha}(r)=&-\frac{r^2}{G(\nu-1)}\left(\frac{r_{,i}r_{,l}}{10}-\frac{9\delta_{li}}{20}+\frac{\delta_{li}\nu}{2}\right)\\&-\frac{r^2}{G\alpha^8(\nu-1)}\left(\frac{7\delta_{li}r^8\nu}{22}-\frac{175\delta_{li}r^8}{572}+\frac{35r_{,i}r_{,l}r^8}{286}\right)\\&+\frac{\alpha r^2}{G\alpha^8(\nu-1)}\left(\frac{32\delta_{li}r^7\nu}{15}-\frac{92\delta_{li}r^7}{45}+\frac{4r_{,i}r_{,l}r^7}{5}\right)\\&+\frac{\alpha^6r^2}{G\alpha^8(\nu-1)}\left(\frac{7\delta_{li}r^2\nu}{5}-\frac{13\delta_{li}r^2}{10}+\frac{2r_{,i}r_{,l}r^2}{5}\right)\\&+\frac{\alpha^3r^2}{G\alpha^8(\nu-1)}\left(8\delta_{li}r^5\nu-\frac{38\delta_{li}r^5}{5}+\frac{14r_{,i}r_{,l}r^5}{5}\right)\\&-\frac{\alpha^4r^2}{G\alpha^8(\nu-1)}\left(5\delta_{li}r^4\nu-\frac{85\delta_{li}r^4}{18}+\frac{5r_{,i}r_{,l}r^4}{3}\right)\\&-\frac{\alpha^2r^2}{G\alpha^8(\nu-1)}\left(\frac{35\delta_{li}r^6\nu}{6}-\frac{245\delta_{li}r^6}{44}+\frac{70r_{,i}r_{,l}r^6}{33}\right)\end{aligned} \tag{31a}$$

4. Method of fundamental solutions for homogeneous solutions

In the MFS, the homogeneous displacement and stress solutions satisfying the homogeneous system consisting of Eqs. (7) and (8) can be approximated by a series of fundamental solutions G_{li}^m, H_{lij}^m with coefficients β_l^m

$$u_i^h(X)=\sum_{m=1}^{M}\beta_l^m G_{li}^m(X) \tag{32a}$$

$$\sigma_{ij}^h(X)=\sum_{m=1}^{M}\beta_l^m H_{lij}^m(X) \tag{32b}$$

where M is number of source points placed outside the domain.

Similar to that in Eq. (15), the fundamental solution G_{li} makes use of Euclidian distance between two points

$$G_{li}^m(X_n)=G_{li}(||X_n-X_m||)=G_{li}(r_{nm}) \tag{33}$$

where X_n represents the collocation points on Γ and X_m represents the source points placed outside Ω.

As is well known in the literature, there is a trade-off between numerical accuracy and stability that the MFS equations could become highly ill-conditioned with increased radial distances in the fundamental solutions [27,31–34]. Usually, the source points can be put on a virtual boundary, which is geometrically similar to the physical boundary of the solution domain. In particular, the source points location can be systematically generated by the following equation [28,35]:

$$X_m = X_n + c(X_n - X_c) \tag{34}$$

where X_c is the centre of Ω and c is a dimensionless parameter to be specified for placing the source points outside Ω. The magnitude of c is a dominant factor of numerical accuracy due to its impact on the radial distances in the fundamental solutions. In our practical computation, the parameter c can be feasibly chosen according to the number of source points to avoid the ill-conditioning of the computing matrix [35,36].

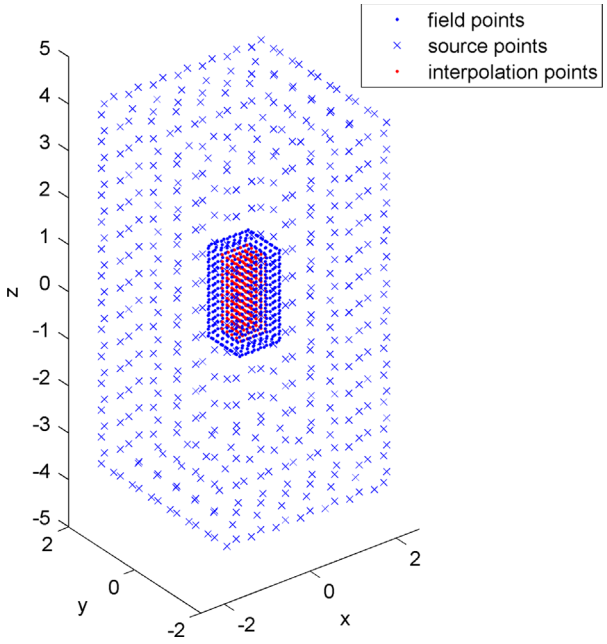

Fig. 3. Distributions of field points, source points and interpolation points for the prismatic bar.

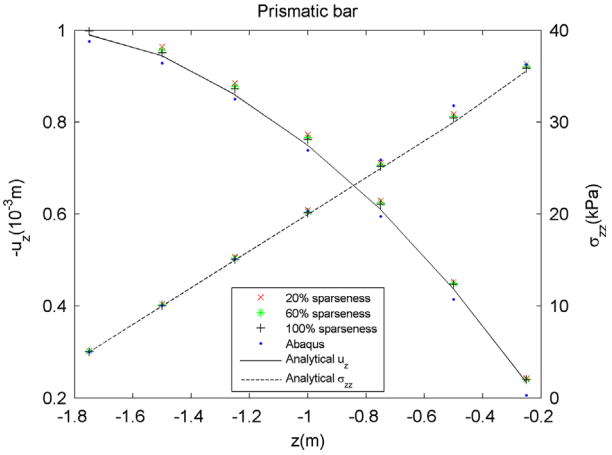

Fig. 4. Displacements and normal stresses along the centreline of the prismatic bar subjected to gravitational load.

Table 1
Displacement results for the prismatic bar.

z (m)	$-u_z$ (10^{-3} m)				
	Present method			**ABAQUS**	**Analytical solutions**
	Sparseness = 20%	Sparseness = 60%	Sparseness = 100%		
−0.25	0.2424	0.2404	0.2397	0.2055	0.2345
−0.50	0.4526	0.4487	0.4471	0.4141	0.4375
−0.75	0.6291	0.6237	0.6211	0.5944	0.6100
−1.00	0.7729	0.7663	0.7627	0.7392	0.7500
−1.25	0.8845	0.8770	0.8726	0.8500	0.8600
−1.50	0.9642	0.9561	0.9511	0.9285	0.9450
−1.75	1.0119	1.0036	0.9982	0.9754	0.9900
MAPE (%)	2.871	2.003	1.552	3.728	

Table 2
Stress results for the prismatic bar numerical simulation.

z (m)	σ_{zz} (kPa)				
	Present method			**ABAQUS**	**Analytical solutions**
	Sparseness = 20%	Sparseness = 60%	Sparseness = 100%		
−0.25	36.34	36.02	35.88	36.30	35.6
−0.50	30.87	30.60	30.44	31.81	30.0
−0.75	25.57	25.35	25.19	25.91	25.0
−1.00	20.42	20.24	20.10	20.31	20.0
−1.25	15.32	15.18	15.06	15.08	15.0
−1.50	10.20	10.13	10.04	10.01	10.0
−1.75	5.11	5.07	5.02	5.00	5.0
MAPE (%)	2.232	1.390	0.673	1.975	

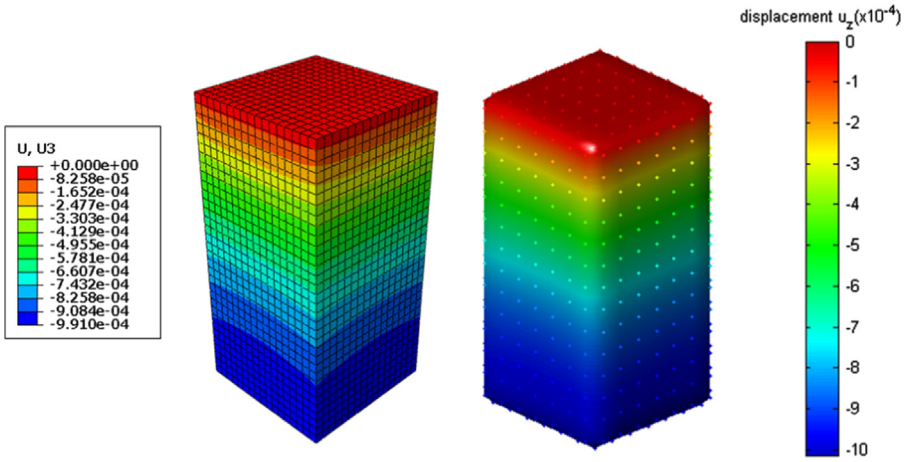

Fig. 5. Contour plots of the vertical displacement component by ABAQUS (left) and the present method (right).

For 3D isotropic linear elastic problems, the fundamental solutions in Eq. (32) is given as [37]

$$G_{li}^{m}(X_n)=\frac{(3-4\nu)\delta_{li}+r_{,l}r_{,i}}{16\pi G(1-\nu)r} \tag{35a}$$

$$H_{lij}^{m}(X_n)=\frac{1}{8\pi(1-\nu)r^2}\left[(1-2\nu)(\delta_{ij}r_{,l}-\delta_{li}r_{,j}-\delta_{lj}r_{,i})-3r_{,l}r_{,i}r_{,j}\right] \tag{35b}$$

From basic definition of fundamental solutions, the homogeneous solutions in Eq. (32) analytically satisfy the homogeneous governing equation (7). Thus, only the modified boundary conditions (8) need to be considered to determine the unknown coefficients β_l^m. For example, by making number of collocation points on the physical boundary Γ equal to the number of source points, we can obtain M linear equations to uniquely solve for the coefficients β_l^m, i.e.

$$\sum_{m=1}^{M}\beta_l^m G_{li}^m(X_k)=\overline{u}_i(X_k)-u_i^p(X_k),\quad X_k\ (1\le k\le N_1)\in\Gamma_u \tag{36a}$$

$$\sum_{m=1}^{M}\beta_l^m H_{lij}^m(X_q)n_j(X_q)=\overline{t}_i(X_q)-t_i^p(X_q),\quad X_q\ (1\le q\le N_2)\in\Gamma_t \tag{36b}$$

where N_1 and N_2 are the numbers of nodes on the displacement boundary Γ_u and the traction boundary Γ_t, respectively. Meanwhile, $M=N_1+N_2$. Finally β_l^m can be determined by solving this square system of linear equations.

5. Numerical examples and discussions

To demonstrate the accuracy and efficiency of the derived formulation, three brenchmark examples, which are solved by the proposed meshless collocation method, are considered in this section. The examples include: (1) a prismatic bar subjected to gravitational load, (2) a cantilever beam under gravitational load, and (3) a thick cylinder under centrifugal load. For simplification, only Wendland's CSRBF with smoothness C^0 is considered here. Simulation results obtained from the proposed method and the conventional FEM method are compared against the analytical solutions. We also compute the mean absolute percentage error (MAPE) as an effective description for quantifying the average performance accuracy of the present method

$$MAPE=\frac{1}{n_t}\sum_{i=1}^{n_t}\left|\frac{(f_{simulation})_i}{(f_{analytical})_i}-1\right|\times 100\% \tag{37}$$

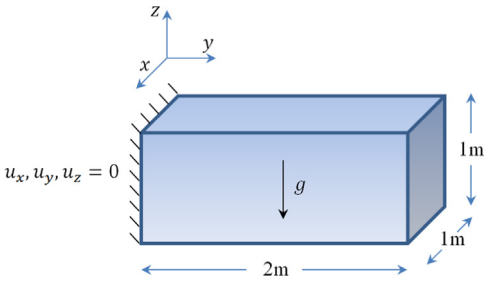

Fig. 6. Bending of cantilever beam under gravitational load.

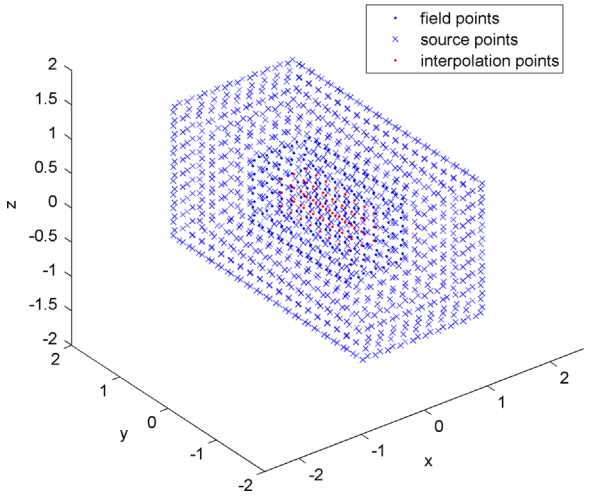

Fig. 7. Distributions of field points, source points and interpolation points for the cantilever.

where $f_{analytical}$ and $f_{simulation}$ are the analytical and simulation values evaluated at test point i. n_t is the total number of the test points.

5.1. Prismatic bar subjected to gravitational load

In the first example, we consider a straight prismatic bar subjected to gravitational load, as shown in Fig. 2. The dimensions of the bar are 1 m × 1 m × 2 m and it is fixed at the top. Assuming the bar being loaded along the z-direction by its gravitational load,

the corresponding body forces can be expressed as

$$b_x = 0, \quad b_y = 0, \quad b_z = \rho g \tag{38}$$

where ρ is density and g is gravity.

The material parameters used in the simulation are: $E = 4 \times 10^7$ Pa, $\nu = 0.25$, $\rho = 2000$ kg m^{-3}, $g = 10$ m s^{-2}. A total number of 490 collocation points are equally spaced on Γ and an additional of 300 points are arranged inside Ω for interpolation using the CSRBF. The number of source points is equal to the number of collocation points on Γ, in which the geometric parameter c of (34) is chosen as 3.0 for the generation of source points, as shown in Fig. 3.

Table 3
Displacement results for the cantilever numerical simulation.

y (m)	u_z (10^{-3} m)			
	Present method			ABAQUS
	Sparseness = 20%	Sparseness = 60%	Sparseness = 100%	
0.25	−0.953	−0.949	−0.940	−0.939
0.50	−2.469	−2.459	−2.436	−2.429
0.75	−4.314	−4.294	−4.253	−4.249
1.00	−6.347	−6.317	−6.254	−6.263
1.25	−8.468	−8.425	−8.340	−8.373
1.50	−10.605	−10.548	−10.440	−10.500
1.75	−12.704	−12.633	−12.501	−12.586

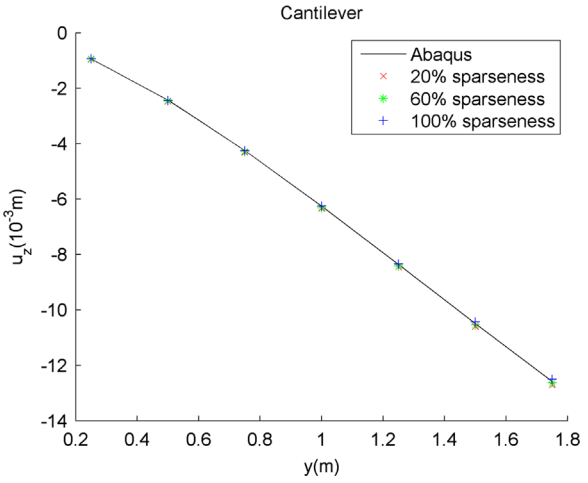

Fig. 8. Displacements along the centre axis of the cantilever subjected to gravitational load.

Test points are chosen along the centreline of the prismatic bar. The corresponding displacement and stress results are compared to the analytical solutions [38,39] and the FEM solutions, which are evaluated by the commercial software Abaqus. Numerical results in Tables 1 and 2 show the variations of displacement and stress in terms of the sparseness of CSRBF. It is found that by increasing the sparseness from 20% to 100%, the MAPE of the present method reduces from 2.87% to 1.55% for the displacement component u_z and from 2.23% to 0.67% for the stress component σ_{zz}. Meanwhile, the MAPE of the Abaqus records at 3.73% and 1.98% respectively. Fig. 4 displays the distribution of displacement and stress components for the sake of clearness. Overall, the present method gives good accuracy and good stability of numerical results for different sparseness values as demonstrated in Tables 1, 2 and Fig. 4. It is noted that in the Abaqus, a total number of 9537 elements of type 20-node quadratic brick are employed for the prismatic bar. Besides, the isoline plot of u_z is provided in Fig. 5, from which a similar colour distribution of the displacement is observed for both the Abaqus and the present method.

5.2. Cantilever beam under gravitational load

Next we consider the bending problem of a cantilever beam under gravitational load. The cantilever beam fixed at $y=0$ is assumed to have dimensions 1 m × 2m × 1 m as shown in Fig. 6. If the gravitational force is along the z-axial direction, the corresponding body forces are the same as those described in Eq. (38).

For the sake of convenience, the material parameters used in the simulation are taken to be the same as those in the first example. A total number of 250 collocation points are equally spaced on the physical boundary and additional 72 interior points are uniformly distributed in the domain for the CSRBF interpolation. However, due to the shear locking, the solving matrix in the MFS could be highly ill-conditioned [40]. To counter this, a number

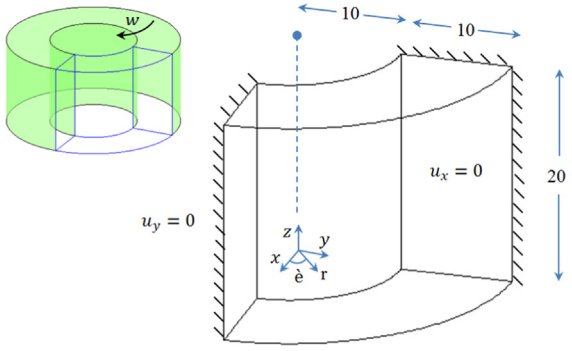

Fig. 10. Thick cylinder under centrifugal load.

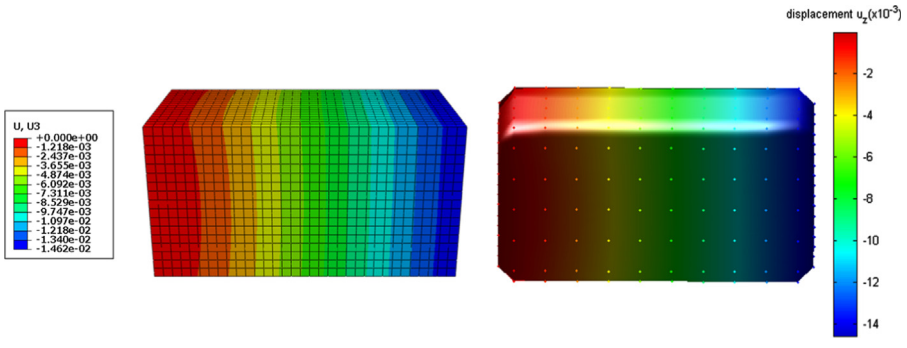

Fig. 9. Contour plots of the displacement results from ABAQUS (left) and the present method (right).

of 1000 source points are generated with geometric parameter $c=1.0$. Fig. 7 displays the geometrical configuration of the source points, collocations and interior interpolation points used in the computation.

To investigate bending shape of the beam, the numerical results of deflection along the y-axis from the present method are compared to those from Abaqus in Table 3. It is found that the numerical results obtained from the various degrees of sparseness do not deviate more than 1.7% from the full sparseness. This implies that the computational accuracy of the present method is not sensitive for low sparseness. The numerical solutions seem to converge when the degree of sparseness increases and the discrepancy between the present method at full sparseness and Abaqus is only 0.32%. For better illustration, the deflection results from the present method are plotted in Fig. 8 and well agreement between the present method and Abaqus is demonstrated. In Abaqus, a total number of 9537 elements of type 20-node quadratic brick elements are employed. Fig. 9 illustrates the isoline maps of the beam deflection from the conventional FEM implemented by Abaqus and the present method, and similar distribution can be observed.

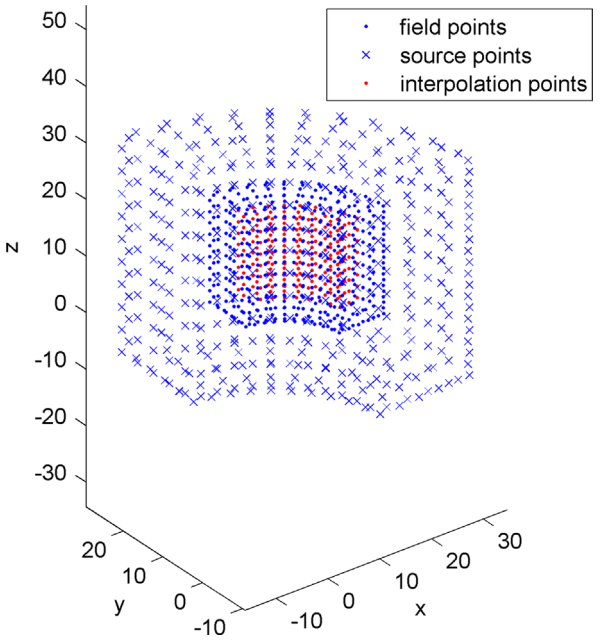

Fig. 11. Distributions of field points, source points and interpolation points for the thick cylinder.

5.3. Thick cylinder under centrifugal load

In the third example, a cylinder with 10 m internal radius, 10 m thickness and 20 m height is assumed to be subjected to centrifugal load. Due to the rotation, this cylinder is subjected to apparent generalised body force. If the cylinder is assumed to rotate about its z-axis as shown in Fig. 10, the generalised body forces in terms of spatial coordinates can be written as

$$b_x = \rho w^2 x, b_y = \rho w^2 y, b_z = 0 \tag{39}$$

where w is the angular velocity. In this example, $w=10$ is chosen.

The problem is solved with dimensionless material parameters $E=2.1\times10^5, v=0.3, \rho=1$. According to the symmetry of the model, only one quarter of the cylinder domain needs to be considered for establishing the computing model. Proper symmetric displacement constraints are then applied on the symmetric planes (see Fig. 10). In the quarter cylinder model, a total number of 430 collocation points are equally spaced on Γ and an additional of 216 points are arranged in Ω for the CSRBF interpolation. For convenience, the number of source points is chosen to be equal to

Table 4
σ_r results for the thick cylinder numerical simulation.

r	σ_r (kPa)					
	Present method				ABAQUS	Analytical solutions
	Sparseness=20%	Sparseness=60%	Sparseness=80%	Sparseness=100%		
11.25	2.723	2.221	2.424	2.340	2.434	2.367
12.50	4.068	3.603	3.673	3.691	3.740	3.620
13.75	4.562	4.247	4.132	4.271	4.233	4.099
15.00	4.482	4.269	4.027	4.245	4.108	4.010
16.25	4.005	3.789	3.489	3.751	3.568	3.484
17.50	3.194	2.902	2.582	2.888	2.647	2.604
18.75	1.942	1.652	1.357	1.684	1.442	1.430
MAPE (%)	17.694	7.492	1.594	7.073	2.394	

Table 5
σ_t results for the thick cylinder numerical simulation.

r	σ_t (kPa)				
	Present method			ABAQUS	Analytical solutions
	Sparseness=20%	Sparseness=60%	Sparseness=100%		
11.25	33.88	28.69	29.92	31.48	30.66
12.50	29.71	26.29	27.00	28.24	27.47
13.75	26.27	24.24	24.53	25.55	24.86
15.00	23.27	22.45	22.38	23.21	22.61
16.25	20.51	20.84	20.43	21.10	20.60
17.50	17.96	19.36	18.63	19.12	18.74
18.75	15.78	18.03	17.05	17.21	16.97
MAPE (%)	5.542	3.520	1.200	2.392	

the number of collocation points on Γ, and their configuration is shown in Fig. 11 by setting the geometric parameter $c=1.0$.

For the rotating cylinder, the displacement and the stress fields are more complicated than those in the straight prismatic bar and the cantilever beam as discussed above. The results of radial and hoop stresses and radial displacement at specified locations are tabulated respectively from the present method (see Tables 4–6). These results are then compared to Abaqus with 10,881 elements of type 20-node quadratic brick elements and the analytical solutions [38,39]. As similar to the former two examples, the MAPE of the present method reduces with increased sparseness. That is, from 17.69% to 7.07% for the radial stress, 5.54% to 1.2% for the hoop stress and 7.69% to 0.09% for the radial displacement while the MAPE of Abaqus is recorded at 2.39% for the stress fields

Table 6
u_r results for the thick cylinder numerical simulation.

r	u_r (m)				
	Present method			ABAQUS	Analytical solutions
	Sparseness=20%	Sparseness=60%	Sparseness=100%		
11.25	1.721	1.562	1.601	1.641	1.604
12.50	1.684	1.531	1.568	1.606	1.571
13.75	1.659	1.509	1.546	1.582	1.547
15.00	1.643	1.491	1.529	1.563	1.529
16.25	1.630	1.474	1.514	1.546	1.513
17.50	1.619	1.455	1.498	1.529	1.497
18.75	1.607	1.432	1.478	1.510	1.477
MAPE (%)	7.692	2.649	0.092	2.225	

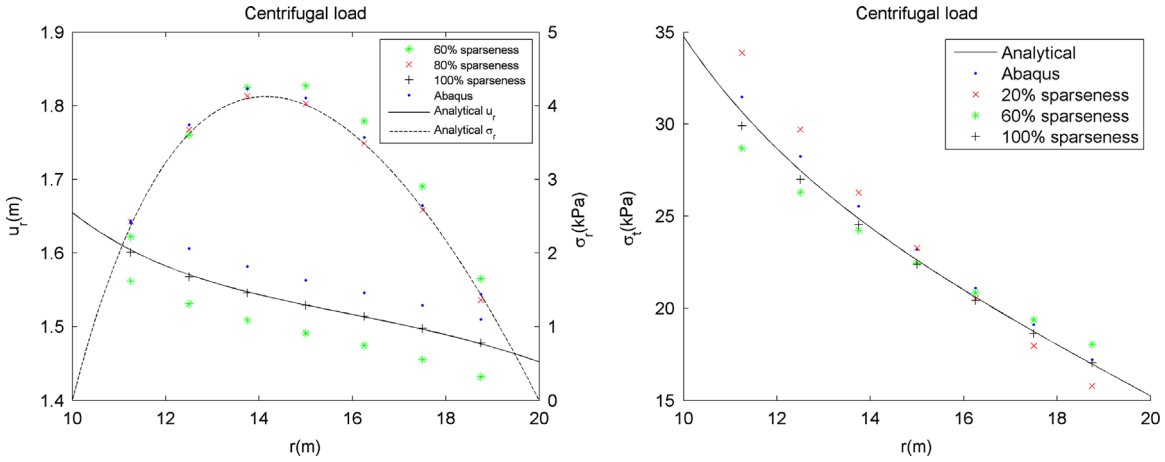

Fig. 12. Plot of radial displacements and radial stresses along the radial direction of the cylinder subjected to centrifugal load (left) and plot of hoop stresses along the same reference locations (right).

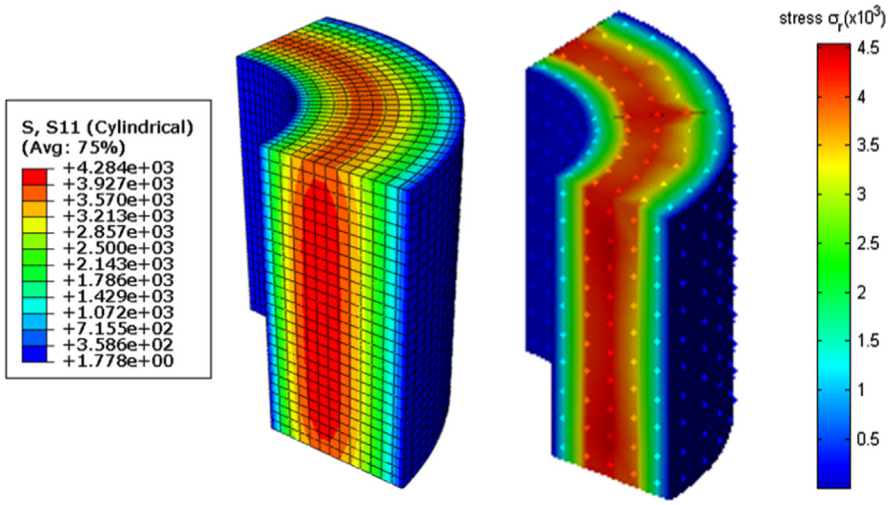

Fig. 13. Contour plots of the σ_r results simulated in Abaqus (left) and the present method (right).

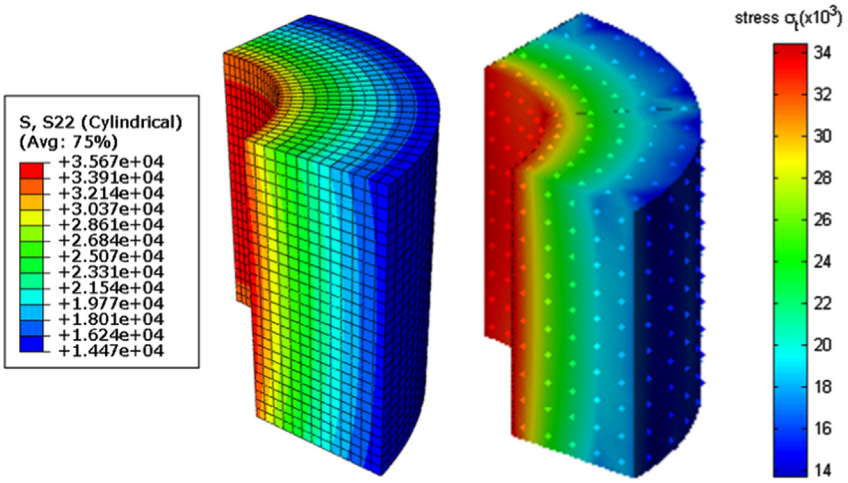

Fig. 14. Contour plot of the σ_t results simulated in Abaqus (left) and the present method (right).

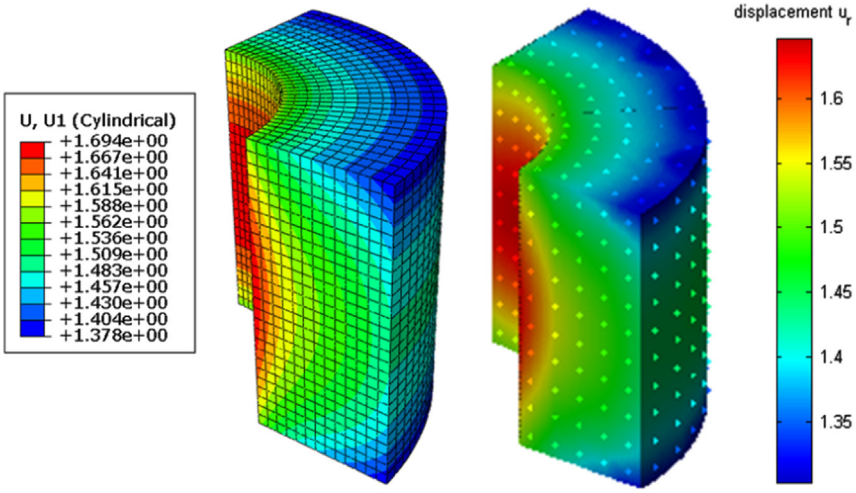

Fig. 15. Contour plot of the u_r results simulated in Abaqus (left) and the present method (right).

and 2.23% for the radial displacement. The present method seems to provide better accuracy for the radial displacement as well as the hoop stress. For the radial stress, an optimal MAPE of 1.59% is found at 80% sparseness of the present method comparing to the 2.39% obtained from the Abaqus. Overall, it is found that reasonable agreement with the analytical solutions is obtained as shown in Fig. 12. The present method with small number of collocations can produce better results than the conventional FEM solutions, which use more elements and nodes, particularly for the case of large sparseness. To investigate the distribution of stresses and displacement in the entire computing domain, some contour plots are given in Figs. 13–15, from which similar variation is observed between Abaqus and the present method.

6. Further discussions on the sparseness of CSRBF

As we know, the merits of using the CSRBF are that the resulting interpolation matrix is sparse for saving computation time and storage. The sparseness of the CSRBF matrix is defined as the cumulative frequency of radial pairs inside the support radius α. As described in Eq. (20), the cumulative frequency plot of radial distance against the normalised radial distance can be computed as shown in Fig. 16. For instance, a 50% sparseness requirement on the quarter cylinder simulation would imply a 0.4 cut off value for

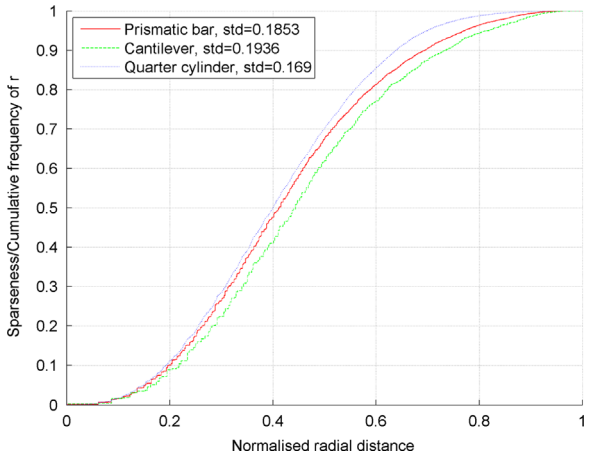

Fig. 16. Cumulative frequency plot of radial distance for prismatic bar, cantilever and quarter cylinder. std is the standard deviation of the radial distance.

α. Since the interpolation points are evenly distributed inside the simulation domains, we anticipate that the standard deviation of the radial distances as well as the sensitivity of α with respect to the sparseness requirement will not differ much for different model geometries.

Besides, sparse matrix could potentially save up computational resources when performing matrix inversion due to the many zero entries enforced on the CSRBF interpolation matrix. Since Wendland's CSRBF is derived to be positive definite, symmetric and sparse [16], Cholesky decomposition can always be employed as an effective mean to factorise the CSRBF matrix φ into upper triangular matrix: $\varphi = U^T U$ for solving the system of linear equations [41]. During the decomposition, however, fill-in may be created resulting in a less sparse system. Reducing the CSRBF matrix fill-in can be achieved by reordering φ of sparse structure before computing the Cholesky decomposition.

Three popular reordering methods, namely the reverse Cuthill–McKee, approximate minimum degree and nested dissection algorithms are chosen to study the effectiveness of minimising the fill-in for the CSRBF matrix. The reverse Cuthill–McKee algorithm seeks to reorder the interpolation matrix with narrow bandwidth [42,43]. The approximate minimum degree algorithm seeks to reorder the matrix with large blocks of continuous zeroes [44,45]. While the minimum degree algorithm prioritises the matrix permutation based on the sparsest pivot row and column, the nested dissection algorithm searches for a node separator, which in turn recursively splits a matrix graph into subgraphs from a top down perspective [46,47]. This paper employs the Matlab build-in functions: *symrcm* and *symamd* to perform the Cuthill–Mckee reordering and the approximate minimum degree reordering respectively. The nested dissection implementation follows the algorithm described by Davis [46]. These three reordering algorithms are employed to illustrate the sparse structures of the CSRBF interpolation matrix and the corresponding Cholesky's upper triangular matrix for the prismatic bar simulation. For the reverse Cuthill–Mckee reordering as shown in the left column of Fig. 17, one can clearly see that the usage of the CSRBF can produce banded interpolation matrix which also results in a banded Cholesky's upper triangular matrix. It is noted that the change of the matrix bandwidth is inversely proportional to the value of the sparseness. In the top centre of Fig. 17, the approximate minimum degree algorithm forms a vastly different pattern of matrix graph as comparing to the former algorithm. There we can see that a lower degree of sparseness (less non-zero entries) tends to produce larger and more blocks of zero entries scattering inside the interpolation matrix. Similarly the nested dissection algorithm produces graph with large blocks of zero entries, in which the non-zero entries are ordered in leaf up shape as shown in the upper right corner of Fig. 17. Neither of the approximate minimum degree nor the nested dissection algorithm produces Cholesky's upper triangular matrix with pattern consistent with the CSRBF matrix before the decomposition (lower mid and lower right of Fig. 17).

To illustrate the effectiveness of each of the reordering algorithms, the sparseness of the Cholesky's upper triangular matrix with respect to the varied sparseness of the CSRBF matrix for the prismatic bar simulation is plotted in Fig. 18. Ideally, the sparseness of the Cholesky's upper triangular matrix is at best equal to the sparseness of the original interpolation matrix provided that there is no fill-in during the Cholesky's decomposition process. Conversely, a full interpolation matrix will result in a full Cholesky's upper triangular matrix. As seen in Fig. 18, CSRBF matrix with sparseness higher than 90% seems to create the same amount of

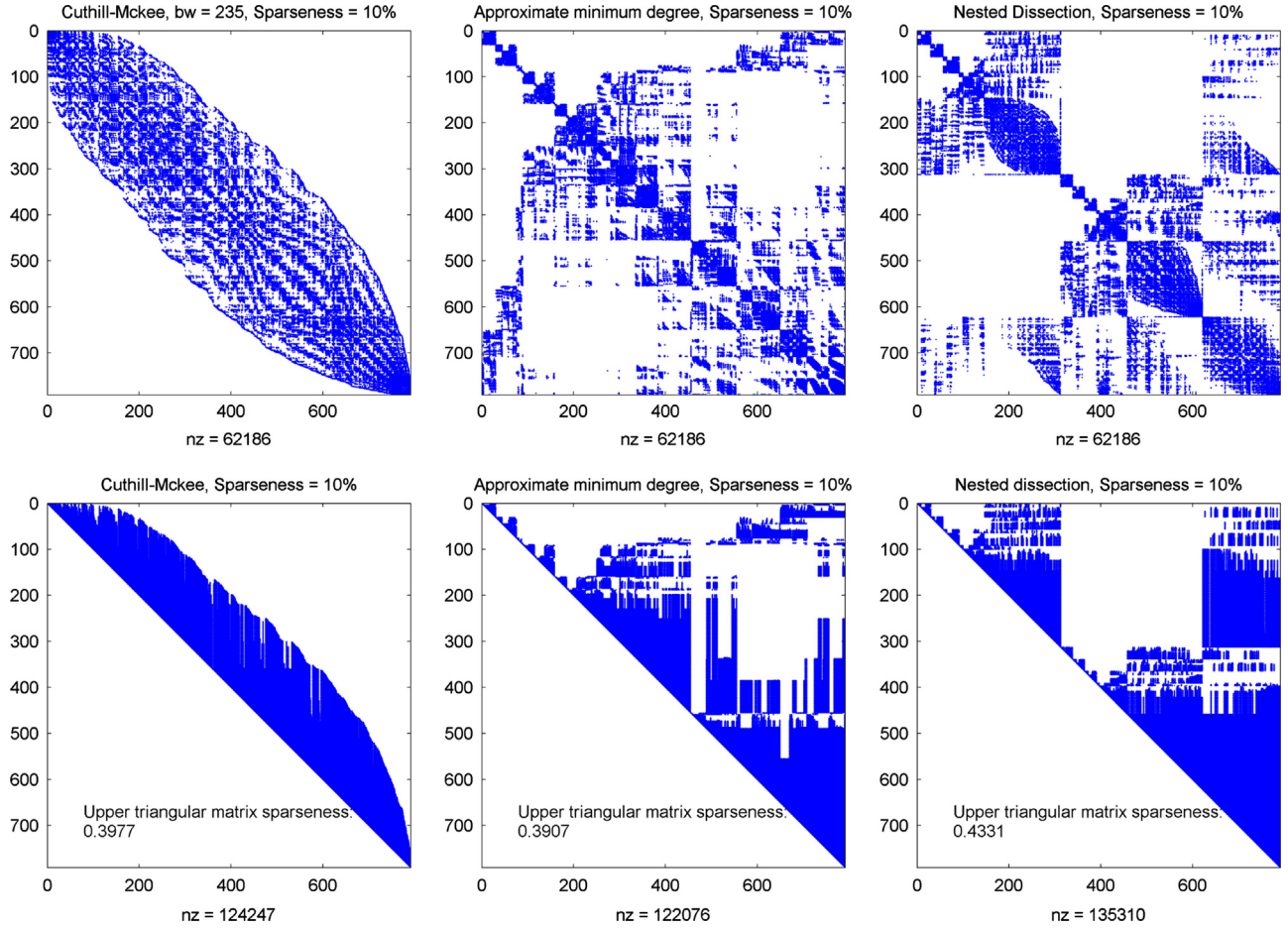

Fig. 17. Structures of the interpolation matrix at 10% sparseness for prismatic bar after reordering using Reverse Cuthill–McKee algorithm (left column), approximate minimum degree (centre column) and nested dissection (right column). First row presents the interpolation matrices after reordering. Second row presents the Cholesky's upper triangular matrices after reordering. bw is the bandwidth and nz is the number of non-zero entries of the matrices.

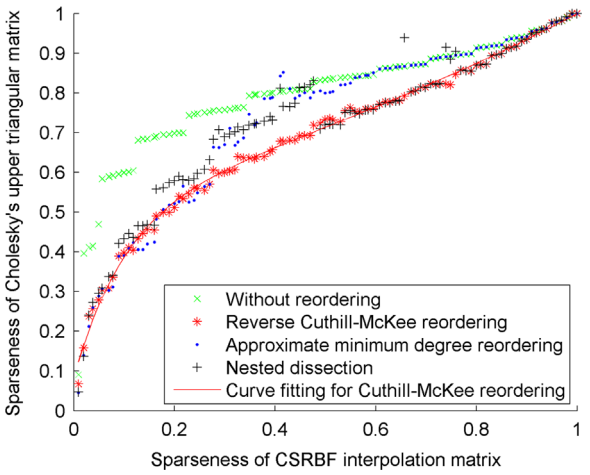

Fig. 18. Varied sparseness of interpolation matrix versus sparseness of Cholesky's upper triangular matrix for prismatic bar after reordering using Reverse Cuthill–McKee algorithm, approximate minimum degree and nested dissection.

fill-in with or without the reordering. For sparseness lower than 90%, Cuthill–Mckee algorithm is capable of reducing the fill-in consistently and noticeably. The approximate minimum degree algorithm seems to be effective for sparseness lower than 40% and could only outperform the Cuthill–Mckee algorithm slightly for very sparse CSRBF matrix, i.e. roughly below 20%. The performance of the nested dissection algorithm is the mix of the former two algorithms. At sparseness 50% or above, its performance follows that of the Cuthill–Mckee algorithm with occasional outliners; for sparseness below 50%, its performance follows that of the approximate minimum degree algorithm with moderate and continuous fluctuations. Sparse matrices with reordering algorithms are generally better than the ones without reordering. This can be observed by comparing the curve without reordering (green scattered crosses) to the very few other points that have worse sparseness in the Cholesky's upper triangular matrix after the reordering. The curves of the Cuthill–Mckee and the approximate minimum degree reordering algorithms can be adequately described by the use of exponential functions: $y = a_1\, e^{a_2 x} + a_3\, e^{a_4 x}$ where a_1, a_2, a_3, a_4 are the coefficients for the curve fitting.

7. Conclusion

In this study, the mixed meshless collocation method is developed through the MFS framework to enrich the application of 3D isotropic linear elasticity with the presence of body forces. The particular solution kernels using the CSRBF interpolation for inhomogeneous body forces are derived using the Galerkin vectors and then coupled with the method fundamental solutions based on a linear combination of fundamental solutions for the full displacement and stress solutions in the solution domain. Numerical results presented in this paper demonstrate that the proposed meshless collocation method is capable of solving three-dimensional solid mechanics problems with inhomogeneous terms efficiently in addition to obtaining high accuracy with varied degrees of sparseness. In contrast to the globally supported RBF, the CSRBF interpolation can provide stable and efficient computational treatment of various body forces. Moreover, the particular solution kernels derived in this paper are directly applicable to the boundary element formulation and other boundary-type methods for determining particular solutions related to inhomogeneous terms in the solution domain.

Acknowledgement

This work is supported by the Australian Research Council (Grant no. DP140103137) and the Natural Science Foundation of China (Grant nos. 11372100 and 11472099).

References

[1] Barber JR. Three-dimensional elasticity solutions for isotropic and generally anisotropic bodies. Appl Mech Mater 2006;5–6:541–50.
[2] Lee CY, Qin QH, Wang H. Trefftz functions and application to 3D elasticity. Comput Assist Mech Eng Sci 2008;15(3–4):251–63.
[3] Piltner R. The use of complex valued functions for the solution of three-dimensional elasticity problems. J Elast 1987;18:191–225.
[4] Qin QH, Mai YW. Crack growth prediction of an inclined crack in a half-plane thermopiezoelectric solid. Theor Appl Fract Mech 1997;26(3):185–91.
[5] Qin QH, Mai YW, Yu SW. Some problems in plane thermopiezoelectric materials with holes. Int J Solids Struct 1999;36(3):427–39.
[6] Qin QH, Zhang X. Crack deflection at an interface between dissimilar piezoelectric materials. Int J Fract 2000;102(4):355–70.
[7] Qin QH. The Trefftz finite and boundary element method. Southampton: WIT Press; 2000.
[8] Bathe KJ. Finite element procedures. Prentice Hall: The University of Michigan; 1996.
[9] Qin QH. Variational formulations for TFEM of piezoelectricity. Int J Solids Struct 2003;40(23):6335–46.
[10] Qin QH. Nonlinear analysis of Reissner plates on an elastic foundation by the BEM. Int J Solids Struct 1993;30(22):3101–11.
[11] Nardini D, Brebbia CA. A new approach to free vibration analysis using boundary elements. Appl Math Model 1983;7(3):157–62.
[12] Golberg MA, Chen CS, Bowman H, Power H. Some comments on the use of radial basis functions in the dual reciprocity method. Comput Mech 1998;22(1):61–9.
[13] Coleman CJ, Tullock DL, Phan-Thien N. An effective boundary element method for inhomogeneous partial differential equations. Z Angew Math Phys 1991;42(5):730–45.
[14] Qin QH, Wang H. Matlab and C programming for Trefftz finite element methods. Boca Raton: CRC Press; 2008.
[15] Natalini B, Popov V. Tests of radial basis functions in the 3D DRM-MD. Commun Numer Methods Eng 2006;22(1):13–22.
[16] Wendland H. Piecewise polynomial, positive definite and compactly supported radial functions of minimal degree. Adv Comput Math 1995;4(1):389–96.
[17] Wendland H. Error estimates for interpolation by compactly supported radial basis functions of minimal degree. J Approx Theory 1998;93(2):258–72.
[18] Chen CS, Kuhn G, Li J, Mishuris G. Radial basis functions for solving near singular Poisson problems. Commun Numer Methods Eng 2003;19(5):333–47.
[19] Golberg MA, Chen CS, Ganesh M. Particular solutions of 3D Helmholtz-type equations using compactly supported radial basis functions. Eng Anal Bound Elem 2000;24(7–8):539–47.
[20] Tsai CC. Meshless BEM for three-dimensional stokes flows. Comput Model Eng Sci 2001;3:117–28.
[21] Rashed YF. Dual reciprocity formulation for elasticity problems using compact supported radial basis functions. In: Breebia CA, Tadeu A, Popov V, editors. Boundary elements XXIV: incorporating meshless solutions; 2002. p. 381–93.
[22] Rashed YF. BEM for dynamic analysis using compact supported radial basis functions. Comput Struct 2002;80(16–17):1351–67.
[23] Chen JS, Wang D, Dong SB. An extended meshfree method for boundary value problems. Comput Methods Appl Mech Eng 2004;193(12):1085–103.
[24] Wang D, Dong SB, Chen JS. Extended meshfree analysis of transverse and inplane loading of a laminated anisotropic plate of general planform geometry. Int J Solids Struct 2006;43(1):144–71.
[25] Fung YC. Foundations of solid mechanics. New Jersey: Prentice-Hall; 1965.
[26] Fam GSA, Rashed YF. The method of fundamental solutions applied to 3D structures with body forces using particular solutions. Comput Mech 2005;36(4):245–54.
[27] Golberg MA, Chen CS. The method of fundamental solutions for potential, Helmholtz and diffusion problems. Bound Integral Methods—Numer Math Asp 1998:103–76.
[28] Wang H, Qin QH. Meshless approach for thermo-mechanical analysis of functionally graded materials. Eng Anal Bound Elem 2008;32(9):704–12.
[29] Buhmann MD. Radial basis functions: theory and implementations. Cambridge: Cambridge University Press; 2003.
[30] Wendland H. Scattered data approximation. Cambridge: Cambridge University Press; 2005.
[31] Barnett AH, Betcke T. Stability and convergence of the method of fundamental solutions for Helmholtz problems on analytic domains. J Comput Phys 2008;227(14):7003–26.
[32] Chen CS, Cho HA, Golberg MA. Some comments on the ill-conditioning of the method of fundamental solutions. Eng Anal Bound Elem 2006;30(5):405–10.
[33] Christiansen S, Meister E. Condition number of matrices derived from two classes of integral equations. Math Methods Appl Sci 1981;3(1):364–92.

[34] Kitagawa T. Asymptotic stability of the fundamental solution method. J Comput Appl Math 1991;38(1):263–9.
[35] Young DL, Jane SJ, Fan CM, Murugesan K, Tsai CC. The method of fundamental solutions for 2D and 3D Stokes problems. J Comput Phys 2006;211(1):1–8.
[36] Wang H, Qin QH. Some problems with the method of fundamental solution using radial basis functions. Acta Mech Sol Sin 2007;20(1):21–9.
[37] Poullikkas A, Karageorghis A, Georgiou G. The method of fundamental solutions for three-dimensional elastostatics problems. Comput Struct 2002;80(3–4):365–70.
[38] Partridge PW, Brebbia CA, Wrobel LC. The dual reciprocity boundary element method. Southampton: Computational Mechanics Publications; 1992.
[39] Sadd MH. Elasticity: theory, applications, and numerics. Academic Press; 2014.
[40] Tiago C, Leitão VMA. Eliminating shear-locking in meshless methods: a critical overview and a new framework for structural theories. Advances in meshfree techniques. Dordrecht: Springer; 2007. p. 123–45.
[41] Rose DJ, Tarjan RE, Lueker GS. Algorithmic aspects of vertex elimination on graphs. SIAM J Comput 1976;5(2):266–83.
[42] Cuthill E, McKee J. Reducing the bandwidth of sparse symmetric matrices. In: Proceedings of the 1969 24th national conference. New York: ACM; 1969. p. 157–72.
[43] Liu WH, Sherman AH. Comparative analysis of the Cuthill–McKee and the reverse Cuthill–McKee ordering algorithms for sparse matrices. SIAM J Numer Anal 1976;13(2):198–213.
[44] Amestoy PR, Davis TA, Duff IS. An approximate minimum degree ordering algorithm. SIAM J Matrix Anal Appl 1996;17(4):886–905.
[45] Markowitz HM. The elimination form of the inverse and its application to linear programming. Manag Sci 1957;3(3):255–69.
[46] Davis TA. Direct methods for sparse linear systems. Philadelphia: SIAM; 2006.
[47] George A. Nested dissection of a regular finite element mesh. SIAM J Numer Anal 1973;10(2):345–63.